Chaos, Solitons & Fractals 75 (2015) 253–262

Contents lists available at ScienceDirect

Chaos, Solitons & Fractals

Nonlinear Science, and Nonequilibrium and Complex Phenomena

journal homepage: www.elsevier.com/locate/chaos

Chaos in Vallis' asymmetric Lorenz model for *El Niño*

B.M. Garay [a,b,*], B. Indig [a,1]

[a] Faculty of Information Technology and Bionics, Pázmány Péter Catholic University, Práter utca 50/A, Budapest H-1083, Hungary
[b] Computer and Automation Institute (SZTAKI), Hungarian Academy of Sciences, Kende u. 13-17, Budapest H-1111, Hungary

ARTICLE INFO

Article history:
Received 5 June 2014
Accepted 19 February 2015
Available online 23 March 2015

ABSTRACT

We consider Vallis' symmetric and asymmetric Lorenz models for *El Niño*—systems of autonomous ordinary differential equations in 3D—with the usual parameters and, in both cases, by using rigorous numerics, we locate topological horseshoes in iterates of Poincaré return maps. The computer-assisted proofs follow the standard Mischaikow–Mrozek–Zgliczynski approach. The novelty is a dimension reduction method, a direct exploitation of numerical Lorenz-like maps associated to the two components of the Poincaré section.

1. Introduction

Consider Vallis' model for *El Niño*

$$\dot{x} = By - C(x+p), \quad \dot{y} = xz - y, \quad \dot{z} = -xy - z + 1 \tag{1}$$

with parameters $B = 102,\ C = 3$ and $p = 0$ in Vallis [1,2] and $B = 102,\ C = 3$ and $p = 0.83$ in Tung [3]. Case $p = 0$ of system (1) can be transformed to the Lorenz system

$$\dot{x} = \sigma(y - x), \quad \dot{y} = rx - y - xz, \quad \dot{z} = xy - bz \tag{2}$$

with $\sigma = C,\ b = 1$, and $r = \frac{B}{C}$ by the following affine substitution [3]:

$$x \to -x, \quad y \to -\frac{C}{B}y, \quad z \to -\frac{C}{B}z + 1.$$

The general analysis of (1) is parallel to the one of the classical Lorenz system (2) in Sparrow [4]. For $a = a(p) > 0$ sufficiently small and $R = R(p) > 0$ sufficiently large, $V(x,y,z) = a(p)x^2 + y^2 + z^2$ defines a quadratic Liapunov function outside the ball of radius R (centered at the origin) and implies that the point at infinity is repulsive. Since the divergence is $-C - 2 < 0$, system (1) admits a compact global attractor $\mathcal{A} = \mathcal{A}_p$ of measure zero. Both for $p = 0$ and $p = 0.83$, system (1) has three equilibria and $\mathcal{A}_p$ looks like an upside down and slightly distorted copy of the standard Lorenz butterfly. For $p \neq 0$, rotation symmetry [5] is broken and one wing becomes less developed than the other. Please see Figs. 1 and 2.

Topological approaches to chaos detection in ordinary differential equations are based on analyzing return maps associated to Poincaré sections. A further dimension reduction, if possible, plays a vital role here.

The aim of the present paper is to provide a computer-assisted proof for chaos in (1), both for $p = 0$ and $p = 0.83$. We follow the Mischaikow–Mrozek–Zgliczynski approach [6–9] for chaos detection in Poincaré return maps. This approach does not require global Poincaré sections. It requires disjoint, carefully selected quadrangles L and R on a carefully selected local Poincaré plane such that the return map on $L \cup R$—in most cases, not the return map itself, but some iterates thereof—is subject to a number of topological constraints.

Preparing for a computer-assisted proof for chaos in system (1), we pass to the set

$$\mathcal{S}(z_0) = \{(x,y,z) \in \mathbb{R}^3 \mid z = z_0 \text{ and } xy < 1 - z_0\}, \tag{3}$$

the subset of the horizontal plane $z = z_0$ where the vector field points upward. The solution flow intersects $\mathcal{S}(z_0)$

* Corresponding author at: Faculty of Information Technology and Bionics, Pázmány Péter Catholic University, Práter utca 50/A, Budapest H-1083, Hungary. Tel.: +36 1 886 4779.
E-mail addresses: garay@digitus.itk.ppke.hu (B.M. Garay), indba@digitus.itk.ppke.hu (B. Indig).
[1] Tel.: +36 1 886 4779.

http://dx.doi.org/10.1016/j.chaos.2015.02.015
0960-0779/

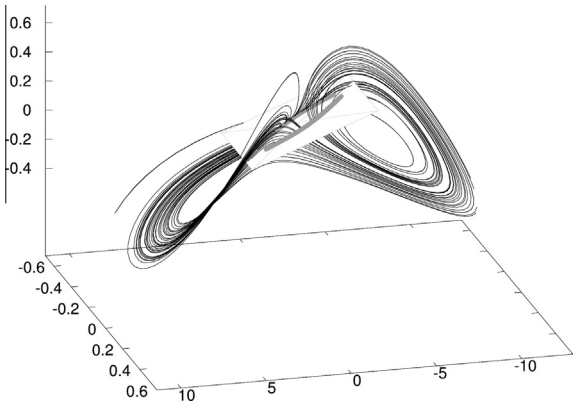

Fig. 1. The horizontal plane $z = 0.3$ intersecting the global attractor $\mathcal{A}_p$, case $p = 0$.

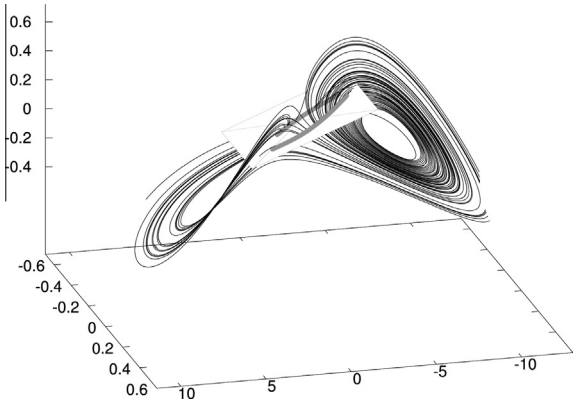

Fig. 2. The horizontal plane $z = 0.3$ intersecting the global attractor $\mathcal{A}_p$, case $p = 0.83$.

transversally and always from the same side, from down to up. For $0 < z_0 < 0.8$, computer simulation suggests that

$$\mathcal{A}_p \cap \mathcal{S}(z_0) = \mathcal{C}_p^u(z_0) \cup \mathcal{C}_p^\ell(z_0), \tag{4}$$

the union of two components. Throughout the present paper, letter $\mathcal{C}$ with superscripts u and ℓ refers not only to a pair of components of a Poincaré section but also to how these components look like, the 'upper curve' and the 'lower curve'.

Though $\mathcal{C}_p^u(z_0)$ and $\mathcal{C}_p^\ell(z_0)$ are dynamically interrelated, we look for chaos on $\mathcal{C}_p^u(z_0)$ and on $\mathcal{C}_p^\ell(z_0)$ separately. When doing this, the representability of $\mathcal{C}_p^u(z_0)$ and $\mathcal{C}_p^\ell(z_0)$ via real functions of the x variable implies that also the (first, the second, and the third iterates of the) return maps can be represented as real functions of the x variable, with a finite number of jump discontinuities. Both for $p = 0$ and $p = 0.83$ with $z_0 = 0.3$, the real functions obtained satisfy the standard Li–Yorke conditions for chaos in one dimension and give rise to the quadrangles L and R needed in the Mischaikow–Mrozek–Zgliczynski approach almost automatically. All in all, they provide a direct link between chaos in one- and in two-dimensional dynamical systems. Our quadrangles L and R are essentially interval segments of the 'curve' $\mathcal{C}_p^u(z_0)$ for $z_0 = 0.3$, slightly thickened in the y direction.

The dimension reduction outlined above has several similarities to the construction of branched manifold models for Lorenz and Rössler type attractors in $\mathbb{R}^3$ [4,10] where monotonicity properties and jump discontinuities of auxiliary functions in one dimension play a key role in explaining the underlying global dynamics [11–13].

The Mischaikow–Mrozek–Zgliczynski approach does not lead to an understanding of the global dynamics. It leads only to results stating that the global dynamics is at least as complicated, say, as the dynamics of the full shift on the space of two symbols.

The paper is organized as follows. The next section begins with recalling the derivation [1] of (1) and ends with some remarks on *El Niño* (*El Niño* Southern Oscillation, ENSO) modeling from the view-point of chaos theory. Concluding Section 2, we report on ordinary and delay equation models demonstrating that existence or nonexistence of chaos depends heavily on discretization and truncation operators chosen. The main result, pointing to a possible difference between the nature of chaos on $\mathcal{A}_p \cap \mathcal{S}(z_0)$ for $z_0 = 0.3$ in the symmetric case $p = 0$ and the asymmetric case $p = 0.83$, is stated as Corollary 1 in Section 3.3. Section 3 begins with motivating the choice $z_0 = 0.3$ and goes on with the definition of the numerical Lorenz-like maps associated to the components of the Poincaré section. Section 4 preceding the Discussion is devoted to the computer-assisted proofs themselves.

2. Chaos in simple models for *El Niño*

The *El Niño* phenomenon is a devilishly irregular, anomalous, Christmas time warming of the coastal waters off Peru and Ecuador about every 3–6 years that has an enormous impact on global climate. Our general reference is the monograph of Sarachik and Cane [14], with a particular emphasis on the *"Noise or chaos? Stable or unstable? Linear or nonlinear? Does it matter and can we tell?"* discussion on pages 280–283.

Vallis model (1) is an $x \sim U$, $y \sim T_e - T_w$, $z \sim T_e + T_w - 2T_d$ affine equivalent form of system

$$\dot{U} = \beta \frac{T_e - T_w}{L} - \gamma(U - U^*) \tag{5}$$

$$Lh \frac{d}{dt} T_w = -Uh \frac{T_w + T_e}{2} + WL \frac{T_w + T_d}{2} - \alpha Lh(T_w - T_*) \tag{6}$$

$$Lh \frac{d}{dt} T_w = Uh \frac{T_w + T_e}{2} - WL \frac{T_e + T_d}{2} - \alpha Lh(T_e - T_*) \tag{7}$$

in the variables U (velocity of the west–east ocean current at the middle of the upper layer) and T_w, T_e (averaged temperatures of the upper ocean layer in the western and eastern Pacific). The ocean current is driven by the surface wind which, in turn, is generated by the temperature gradient. The symmetry between upwelling and downwelling is the result of mass conservation, implying also that $W(t)L = U(t)h$ for each $t \in \mathbb{R}$. Deep ocean temperature under the thermocline is taken for $T_d = \text{const}$. Correction

terms express Newtonian damping. The general setting is shown in Fig. 3.

Though (1) is only a toy model for *El Niño*, the parameter triplets $B = 102,\ C = 3,\ p = 0$ in Vallis [1,2] and $B = 102,\ C = 3,\ p = 0.83$ ($\iff U^* = -2075\frac{km}{month}$, the average effect of trade winds) in Tung [3] carry some physical meaning. Also the chaotic simulations in [2,3] are not absolutely incompatible with *El Niño* observations.

Eqs. (6) and (7) without the damping terms describe heat exchange between the three ocean segments considered. This part of system (5)–(7) can be obtained from the 2D heat advection equation $\frac{\partial T}{\partial t} = -\frac{\partial(uT)}{\partial x} - \frac{\partial(wT)}{\partial z}$ via two-point centered finite differences. However, existence or non-existence of chaos depends on the grid and the discretization method chosen. As Vallis [2] himself observes, a two-point upwind scheme results in an apparently bisTable 3D system of ordinary differential equation modeling *El Niño*.

Thus the situation is the same as with the derivation of the classical Lorenz equations. System (2) is obtained via keeping the first three coefficients in a double Fourier expansion when solving the convection equations of Saltzman. Depending on which Fourier modes are kept, the qualitative properties of the approximating systems of ordinary differential equations differ considerably. Not all of them are chaotic and even if chaotic, the dynamical behavior at the onset of chaos varies on a case to case basis. This is a widely studied area of research [2,15].

Concluding this section, some recent results on delay equation models for *El Niño* dynamics are reported. Both in the Suarez–Schopf model [16]

$$\dot{x}(t) = x(t) - \alpha x(t-\tau) - x^3(t) \tag{8}$$

and in the Battisti–Hirst model [17]

$$\dot{x}(t) = x(t) - \alpha x(t-\tau) - \beta(x(t) - \gamma x(t-\tau))^3, \tag{9}$$

$x = x(t)$ can be roughly identified with $T_e = T_e(t)$. Clearly Eq. (8) is the $\beta = 1, \gamma = 0$ special case of Eq. (9). By a theorem of Tibor Krisztin [18], an application of the Poincaré–Bendixson type theorem of Mallet–Paret and Sell [19], the existence of a compact global attractor in Eq. (8) is proven but the existence of chaos is excluded, for all reasonable parameter values. On the other hand, when equipped with the original parameters, Eq. (9) seems to be chaotic [20]. This latter claim is supported by strong numerical evidence.

3. Connecting chaos in one and two dimensions

Now we return to (3) and (4) and take $z_0 = 0.3$ in the sequel.

3.1. Motivating the choice for z_0

The return map as a self-map of $\mathcal{C}_p^u(z_0)$ is defined by restricting the return map to the maximum possible subset of $\mathcal{C}_p^u(z_0)$ with the property that both domain and range are subsets of $\mathcal{C}_p^u(z_0)$. Chaos on $\mathcal{C}_p^u(z_0)$ is understood in the sense of chaos for (iterates of) the return map as a self-map of $\mathcal{C}_p^u(z_0)$.

In order to select a value for z_0, it is important for us that—forgetting about the Cantor book structure—both $\mathcal{C}_p^u(z_0)$ and $\mathcal{C}_p^\ell(z_0)$ are representable as graphs of continuous real functions of the x variable. For $0 < z_0 < 0.26$, the left end of $\mathcal{C}_p^u(z_0)$ and the right end of $\mathcal{C}_p^\ell(z_0)$ fold back and make such a simple representation impossible. Please see the left panel of Fig. 4 presenting $\mathcal{A}_0 \cap \mathcal{S}(z_0)$ for $z_0 = \frac{1}{34}$, the plane containing also the pair of equilibria $\left(\pm\sqrt{33}, \pm\frac{\sqrt{33}}{34}, \frac{1}{34}\right)$. The folds disappear for $0.27 < z_0 < 0.8$. The right panel of Fig. 4 shows $\mathcal{C}_{0.83}^u(z_0)$ and $\mathcal{C}_{0.83}^\ell(z_0)$ for $z_0 = 0.3$.

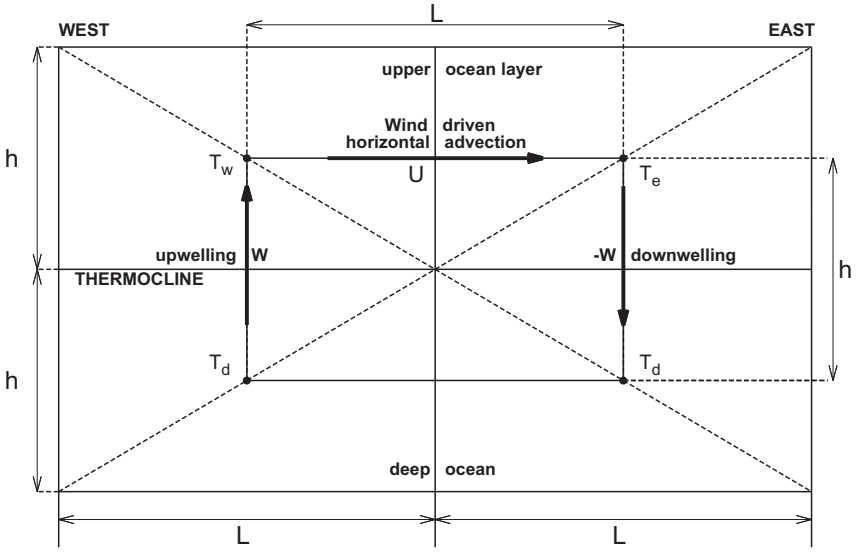

Fig. 3. Vallis' model for heat fluctuations in the west–east section of the equatorial Pacific. Here L is taken for 7500 km but the value of h does not need to be specified.

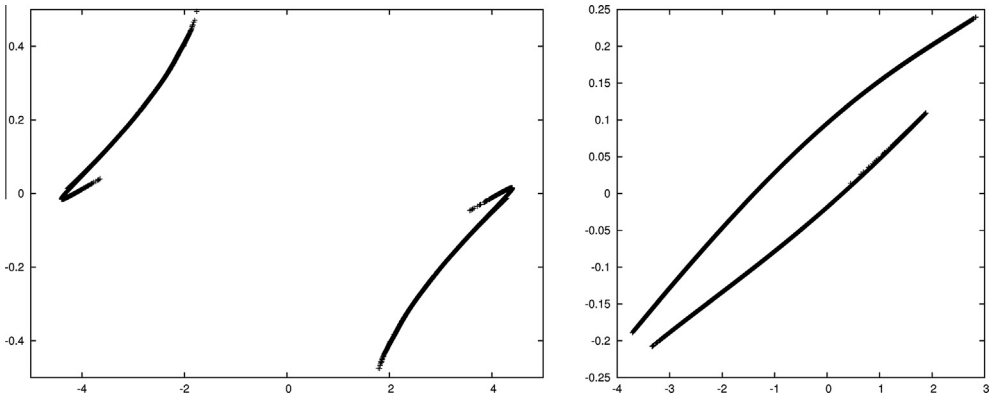

Fig. 4. $\mathcal{A}_0 \cap \mathcal{S}(\frac{1}{34}) = \mathcal{C}_0^u(\frac{1}{34}) \cup \mathcal{C}_0^\ell(\frac{1}{34})$ with the folds (left panel) and $\mathcal{A}_{0.83} \cap \mathcal{S}(0.3) = \mathcal{C}_{0.83}^u(0.3) \cup \mathcal{C}_{0.83}^\ell(0.3)$ represented as the union of graphs of the continuous real functions $y = \mathfrak{m}_{0.83}^u(x)$ and $y = \mathfrak{m}_{0.83}^\ell(x)$ (right panel).

The main reason for letting $z_0 = 0.3$ is demonstrated in Fig. 5 portraying the second iterate of the return map as a self-map of $\mathcal{C}_0^u(z_0)$ for $z_0 = 0.272,\ z_0 = 0.286$, and $z_0 = 0.3$ in a vicinity of fixed points. There is a unique fixed point for $z_0 = 0.272$. Observe the development of the continuous, increasing branches resulting in additional fixed points for $z_0 = 0.3$. The crucial part of (the right panel of) Fig. 5 is shown on the right panel of Fig. 6 as well. The continuous, increasing branches about the fixed points at $x = -1.847\ldots$ and $x = -1.696\ldots$ are long enough to open up the possibility of applying Theorem 1 below, a central result of the Mischaikow–Mrozek–Zgliczynski approach.

3.2. The definition of the numerical Lorenz-like maps

Recalling (3) and (4) again, we set

$$\mathcal{S} = \{(x, y, 0.3) \in \mathbb{R}^3 \mid xy < 0.7\}.$$

For $p = 0$ and $p = 0.83$, the upper part and the lower part of $\mathcal{S}$ are defined by using a separation line $y - y_p = m_p(x - x_p)$ we specify first. Let

$$(x_p, y_p, m_p) = \begin{cases} (3.202, 0.207, 0.06402) & \text{if } p = 0 \\ (2.855, 0.209, 0.06389) & \text{if } p = 0.83 \end{cases}$$

and take

$$\mathcal{S}_p^u = \{(x, y, 0.3) \in \mathcal{S} \mid y - y_p > m_p(x - x_p)\},$$

$$\mathcal{S}_p^\ell = \{(x, y, 0.3) \in \mathcal{S} \mid y - y_p < m_p(x - x_p)\}.$$

For the purposes of the present paper, the set $\mathcal{A}_p \cap \mathcal{S}$ is represented by the tail of the sequence of consecutive upward numerical intersections between the trajectory starting from the point $P^* = (0.5, 1, 0.3) \in \mathcal{S}$ and the plane of equation $z = 0.3$. More precisely, forgetting about the last coordinate of the kth upward numerical intersection point (the kth numerical iterate of P^* under the return map Π_p on the Poincaré section).

$$\Pi_p^k(P^*) = \left(x_p^k, y_p^k, z_p^k\right) = \left(x_p^k, y_p^k, 0.3\right) \in \mathcal{S},$$

the set $\mathcal{A}_p \cap \mathcal{S}$ is visualized by the finite sequence

$$\left(x_p^k, y_p^k\right) \in \mathbb{R}^2, \quad k = 50, 51, \ldots, 100000.$$

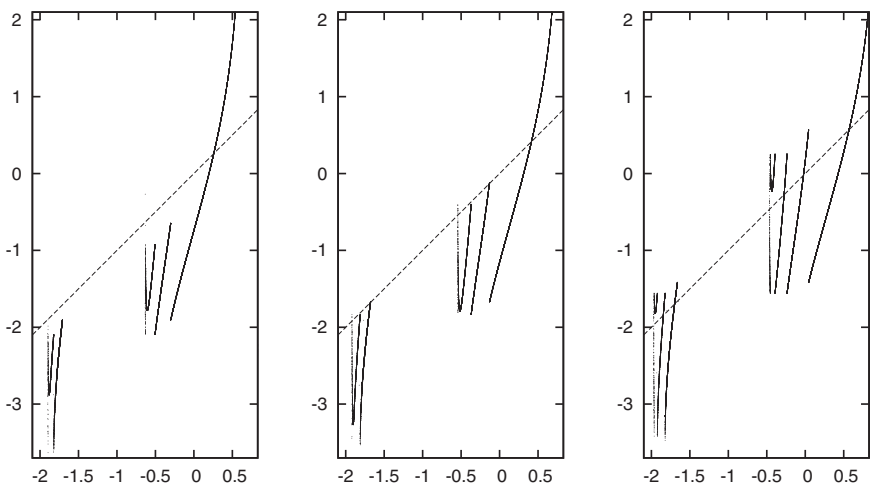

Fig. 5. The creation of additional fixed points on $\mathcal{C}_0^u(z_0)$ for the second return map as z_0 reaches 0.3 from below: $z_0 = 0.272$ (left panel), $z_0 = 0.286$ (middle panel), and $z_0 = 0.3$ (right panel).

From now on, parameter values $p = 0$ and $p = 0.83$ will be referred to by subscripts S and A (symmetry versus asymmetry), respectively. The upper part and the lower part of $\mathcal{A}_I \cap \mathcal{S}$ are defined as

$$\mathcal{C}_I^u = \mathcal{A}_I \cap \mathcal{S}_I^u, \quad \mathcal{C}_I^\ell = \mathcal{A}_I \cap \mathcal{S}_I^\ell, \quad I = S, A. \tag{10}$$

With a good approximation, $\mathcal{C}_I^i$ can be represented as the graph of a continuous function $y = \mathfrak{m}_I^i(x), i = u, \ell$.

For $n = 1, 2, 3$ (there is no need of going any further), a four-member collection of numerical Lorenz-like maps

$$M_{I,n}^i : x_I^k \to x_I^{k+n}, \quad i = u, \ell \quad \text{and} \quad I = S, A \tag{11}$$

is introduced, simply by specifying the respective domains. For $i = u, \ell$ and $I = S, A$, the domain of $M_{I,n}^i$, $n = 1, 2, 3$ is chosen for the subsequence of x_I^k with indices $50 \leqslant k \leqslant 100000 - n$ such that

$$(x_I^k, y_I^k, 0.3) \in \mathcal{S}_I^i \quad \text{and} \quad (x_I^{k+n}, y_I^{k+n}, 0.3) \in \mathcal{S}_I^i.$$

Though its domain consists of only a finite set of points, we consider $M_{I,n}^i$ as if it were defined and continuous on a finite union of open intervals. This heuristics is made possible by the relative denseness of the actual domains.

Remark 1. Both for $I = S$ and $I = A$, the Poincaré return map Π_I on $\mathcal{C}_I^u \cup \mathcal{C}_I^\ell$ falls apart as the four-member collection of mappings

$$\Pi_{I,i\to j} : \mathcal{C}_I^i \to \mathcal{C}_I^j \quad \text{where} \quad i, j = u, \ell. \tag{12}$$

The concept of iterates of the Poincaré return map as a self-map of $\mathcal{C}_I^i$ $(i = u, \ell)$ is closely connected to the separation of cases considered in (12). For example, the second return map as a self-map of $\mathcal{C}_I^u$ is the union of the composite functions

$$\Pi_{I,u\to u} \circ \Pi_{I,u\to u} \quad \text{and} \quad \Pi_{I,\ell\to u} \circ \Pi_{I,u\to \ell}$$

with maximum possible domains. The definition of what we call numerical Lorenz-like maps $M_{I,n}^i$ $(i = u, \ell,\ I = S,\ A,\ n = 1, 2, 3)$ in (11) follows the same logic. The terminology refers to the Lorenz cusp map as to the prototype of auxiliary real functions for studying chaos in higher dimensions.

The graphs of mappings $M_{S,2}^u$, $M_{A,3}^u$, $M_{S,1}^u$ & $M_{S,1}^\ell$ and $M_{A,2}^u$ & $M_{A,2}^\ell$ are shown in Figs. 6, 9, 11 and 12, respectively. Both horizontally and vertically, the plotting range in all these Figures is the interval $[-4, 4]$.

3.3. The main results of the present paper

Lorenz-like maps as defined above imply quite easily the following result on Eq. (1) with parameters $B = 102$, $C = 3$ and $p = 0$ (the symmetric case $I = S$) or $p = 0.83$ (the asymmetric case $I = A$).

Corollary 1. *Mapping Π_S^2 (the second iterate of the return map) admits a Σ_2-chaos on the 'upper curve' $\mathcal{C}_S^u$ defined in (10). Mapping Π_A^3 admits a Σ_2-chaos on $\mathcal{C}_A^u$.*

Corollary 1 is derived as an application of the following version of a theorem by Zgliczynski [8]. (A simple proof of Theorem 1, based on Brouwer's fixed point theorem, can be found in [21].)

Theorem 1. Set $X = \mathbf{R}^2$. With $x = (x_1, x_2) \in \mathbf{R} \times \mathbf{R} = X$, define

$$E = \{x \in X \mid 1 \leqslant |x_1| \leqslant 2, |x_2| \geqslant 2\}, \quad O_C = \{x \in X \mid |x_1| < 1\},$$

$$R = \{x \in X \mid 1 \leqslant x_1 \leqslant 2, |x_2| \leqslant 2\}, \quad O_R = \{x \in X \mid x_1 > 2\},$$

$$L = \{x \in X \mid -2 \leqslant x_1 \leqslant -1, |x_2| \leqslant 2\},$$
$$O_L = \{x \in X \mid x_1 < -2\},$$

$$a = R \cap \mathrm{cl}(O_R), \quad b = R \cap \mathrm{cl}(O_C), \quad c = L \cap \mathrm{cl}(O_C),$$
$$d = L \cap \mathrm{cl}(O_L).$$

Consider a homeomorphism φ of $L \cup R$ onto $\varphi(L \cup R)$ and suppose that

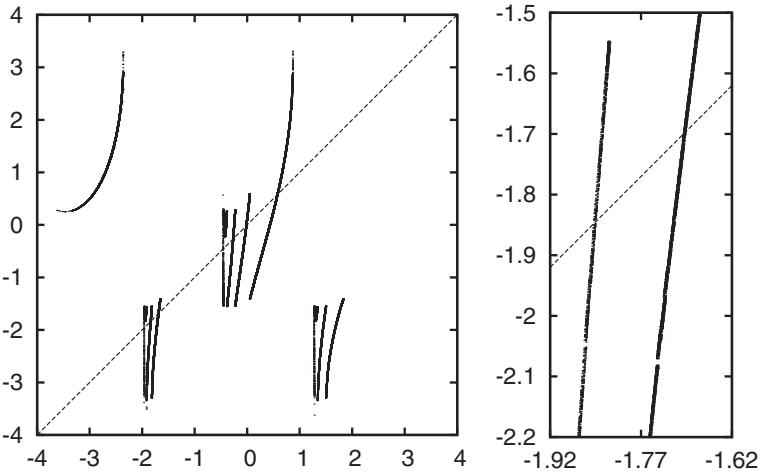

Fig. 6. The graph of $M_{S,2}^u$, with a magnified and rescaled view of a selected area (for determining the values of δ, γ, β and α in (15)).

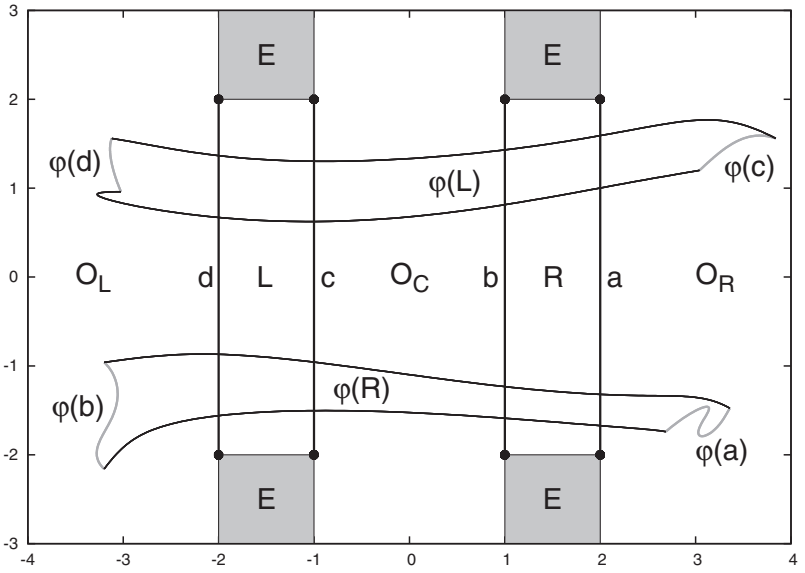

Fig. 7. The setting of Theorem 1.

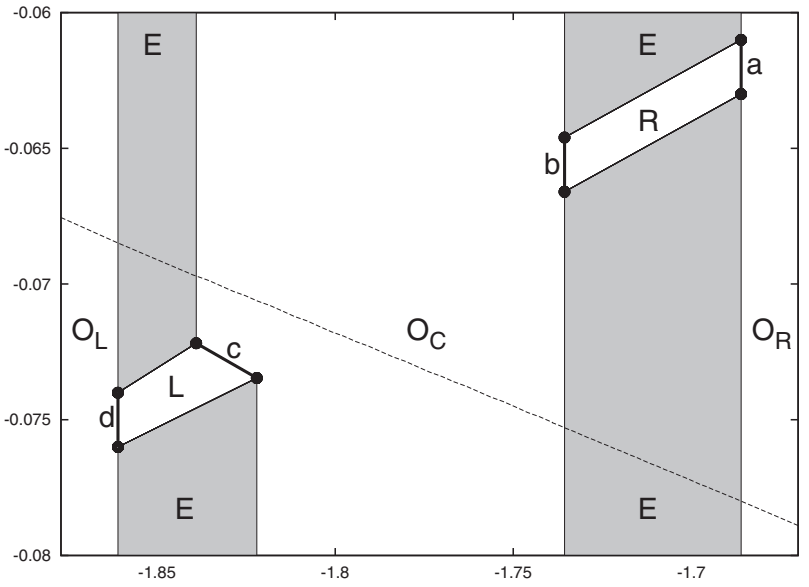

Fig. 8. The final quadrangles in proving the first part of Corollary 1. The almost straight dashed line between L and R shows a portion of $\mathcal{S} \cap \mathcal{M}^s(0,0,1)$, the intersection between $\mathcal{S}$ and the stable manifold of equilibrium $(0,0,1) \in \mathbb{R}^3$.

$$\varphi(a) \cup \varphi(c) \subset O_R, \quad \varphi(b) \cup \varphi(d) \subset O_L, \quad \text{and} \quad \varphi(L \cup R) \subset X \setminus E. \tag{13}$$

Then mapping

$$\sigma : \Lambda_\varphi = \mathrm{cl}(\{\varphi\text{-periodic points with trajectories in } L \cup R\}) \to \Sigma_2$$

defined by

$$(\sigma(x))_k = \begin{cases} 0 & \text{whenever } \varphi^k(x) \in L \\ 1 & \text{whenever } \varphi^k(x) \in R \end{cases} \quad \text{for each } x \in \Lambda_\varphi,\ k \in \mathbb{Z}$$

is continuous, onto and satisfies $\sigma\varphi = S\sigma$ *on* Λ_φ. *In particular,* $\varphi|_{\Lambda_\varphi} : \Lambda_\varphi \to \Lambda_\varphi$ *is semiconjugate to* $S : \Sigma_2 \to \Sigma_2$, *the shift operator on the space of two symbols (the space of doubly infinite 0–1 sequences equipped with the product topology).*

Any application of Theorem 1 involves a setting homeomorphic to the horizontal–vertical setting in Fig. 7. Rectangles L and R are typically replaced by quadrangles with no horizontal or vertical sides. In our case, proving the first part of Corollary 1, intervals supporting the continuous, increasing branches about the fixed points $x = -1.847\ldots$ and $x = -1.696\ldots$ in Fig. 6 are instrumental.

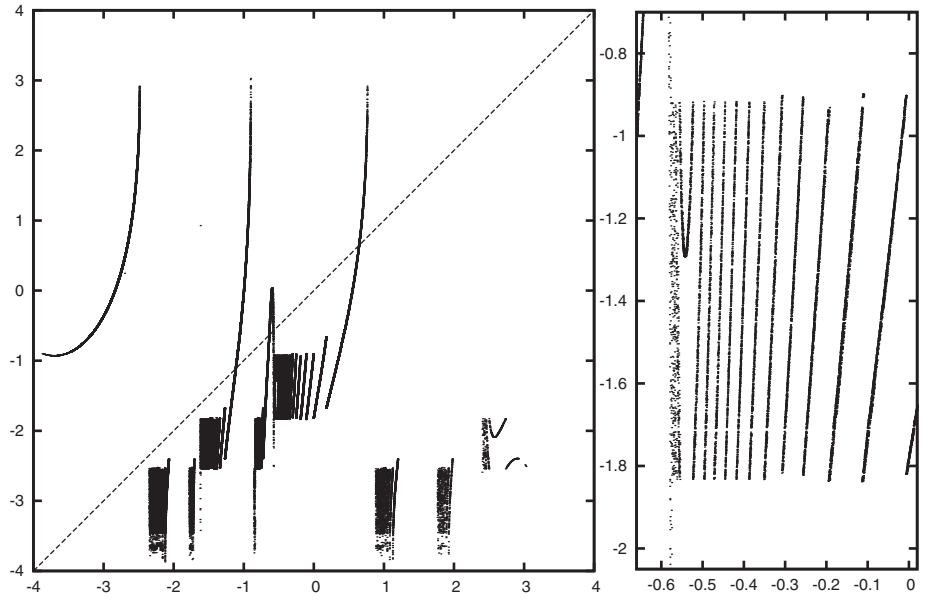

Fig. 9. The graph of M^u_{A3}, with a magnified and rescaled view of a selected area (the values of $\delta \approx -1.2, \gamma \approx -0.97, \beta \approx 0.25$ and $\alpha \approx 0.7$) can be read from the left panel of the figure.

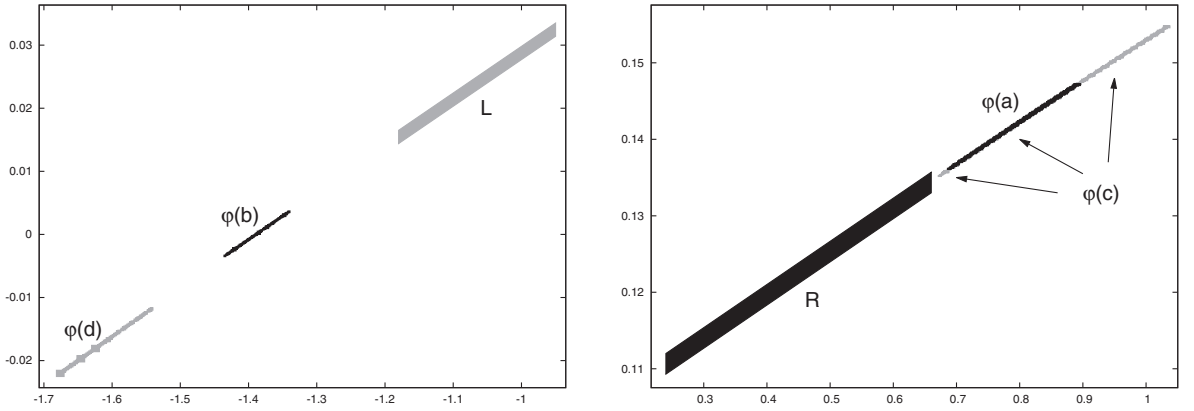

Fig. 10. The final quadrangles L and R in proving the second part of Corollary 1, together with the images of the vertical segments **a**, **b**, **c**, **d**.

In the final analysis, they correspond to the two symbols of the full shift.

Inspecting the right panel of Fig. 6, our first choice for L and R are

$$L_{init} = \mathrm{conv}\{\mathbf{d}_{init}, \mathbf{c}_{init}\},\ R_{init} = \mathrm{conv}\{\mathbf{b}_{init}, \mathbf{a}_{init}\} \tag{14}$$

with vertical sides

$$\mathbf{a}_{init} = \{\alpha\} \times [m^u_S(\alpha) - \varepsilon, m^u_S(\alpha) + \varepsilon],$$

$$\mathbf{b}_{init} = \{\beta\} \times [m^u_S(\beta) - \varepsilon, m^u_S(\beta) + \varepsilon],$$

$$\mathbf{c}_{init} = \{\gamma\} \times [m^u_S(\gamma) - \varepsilon, m^u_S(\gamma) + \varepsilon],$$

$$\mathbf{d}_{init} = \{\delta\} \times [m^u_S(\delta) - \varepsilon, m^u_S(\delta) + \varepsilon],$$

respectively. Here $\delta = -1.86,\ \gamma = -1.82,\ \beta = -1.73,\ \alpha = -1.68$ (with $\delta, \gamma, \beta, \alpha$ belonging to the domain of $M^u_{S,2}$ and constant $0 < \varepsilon \ll 1$ has still to be specified. The idea is if we had a continuous function $M : [\delta, \gamma] \cup [\beta, \alpha] \to \mathbb{R}$ with the properties that

$$M([\delta, \gamma]) \supset [\delta, \gamma] \cup [\beta, \alpha], \quad M([\beta, \alpha]) \supset [\delta, \gamma] \cup [\beta, \alpha] \tag{15}$$

(a Li–Yorke sufficient condition for chaos in one dimension) and that both $M|_{[\delta,\gamma]}$ and $M|_{[\beta,\alpha]}$ were strictly increasing.

Borrowing a term from the theory of global optimization, the quadrangles in (14) serve as an educated initial guess for a successful application of Theorem 1. The final quadrangles are shown in Fig. 8. The unbounded sides of the taboo set E are kept vertical.

4. The proof of Corollary 1

From a purely theoretical view-point, the problem of finding the appropriate quadrangles that satisfy condition

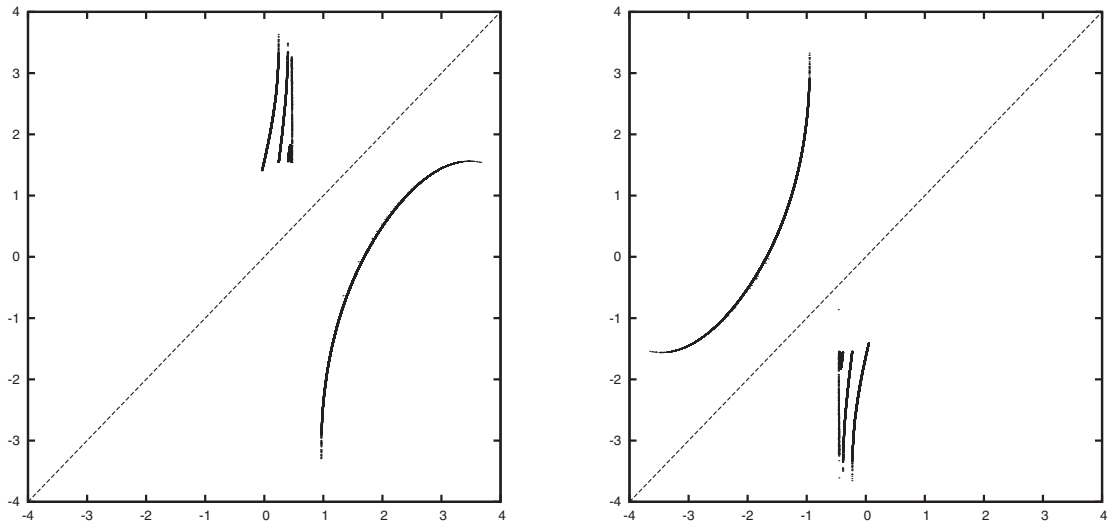

Fig. 11. The graphs of the Lorenz-like maps $M^{\ell}_{S,1}$ (left panel) and $M^{u}_{S,1}$ (right panel): no fixed points at all.

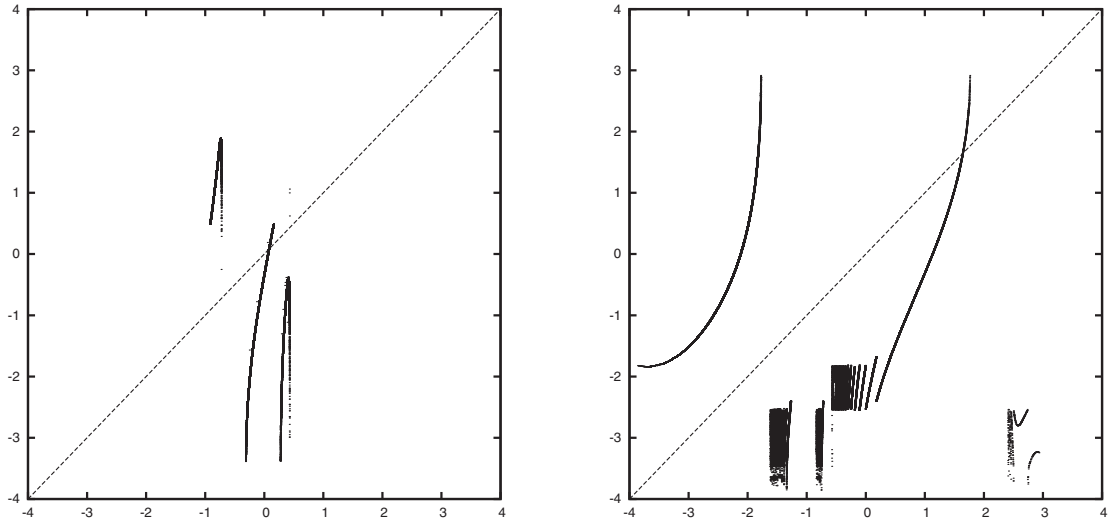

Fig. 12. The graphs of the Lorenz-like maps $M^{\ell}_{A,2}$ (left panel) and $M^{u}_{A,2}$ (right panel): only one fixed point in both cases.

(13) is a constraint satisfaction problem in rigorous global optimization. Requiring that the eight half-lines (determining the taboo set E) are all vertical, one has to work with 16 parameters, the coordinates of the vertices of two general quadrangles L and R. With $\varepsilon = 0.01$, parallelograms L_{init} and R_{init} in (14) can serve as initial data for this procedure. Though the method works for iterates of the classical Hénon mapping [21], its combination with a rigorous ODE solver seems to be too involved for us. We follow the pedestrian approach instead and refine L_{init} and R_{init} by nonrigorous and nonautomatic methods. Having arrived at a "truly promising" pair of candidates for L and R, we pass to rigorous computation and check if condition (13) is satisfied or not. If not, then the entire process is reiterated until condition (13) is checked for the final quadrangles L and R.

As for the first part of Corollary 1, we set

$$\varphi = \Pi_S^2, \quad L = \mathrm{conv}\{\mathbf{d}, \mathbf{c}\}, \quad R = \mathrm{conv}\{\mathbf{b}, \mathbf{a}\} \tag{16}$$

with the straight line segments $\mathbf{d}, \mathbf{c}, \mathbf{b}, \mathbf{a} \subset \mathcal{S}$ chosen for

$$\mathbf{a} = \mathrm{conv}\{(-1.686, -0.061, 0.3), (-1.686, -0.063, 0.3)\},$$
$$\mathbf{b} = \mathrm{conv}\{(-1.7356, -0.0646, 0.3), (-1.7356, -0.0666, 0.3)\},$$
$$\mathbf{c} = \mathrm{conv}\{(-1.839, -0.07218, 0.3), (-1.822, -0.07346, 0.3)\},$$
$$\mathbf{d} = \mathrm{conv}\{(-1.861, -0.074, 0.3), (-1.861, -0.076, 0.3)\}.$$

See Fig. 8 again.

As for the second part of Corollary 1, we set

$$\varphi = \Pi_A^3, \quad L = \mathrm{conv}\{\mathbf{d}, \mathbf{c}\}, \quad R = \mathrm{conv}\{\mathbf{b}, \mathbf{a}\} \tag{17}$$

with the straight line segments $\mathbf{d}, \mathbf{c}, \mathbf{b}, \mathbf{a} \subset \mathcal{S}$ chosen for

$$\mathbf{a} = \mathrm{conv}\{(0.66, 0.133, 0.3), (0.66, 0.1357, 0.3)\},$$
$$\mathbf{b} = \mathrm{conv}\{(0.24, 0.1093, 0.3), (0.24, 0.112, 0.3)\},$$
$$\mathbf{c} = \mathrm{conv}\{(-0.95, 0.0314, 0.3), (-0.95, 0.0335, 0.3)\},$$
$$\mathbf{d} = \mathrm{conv}\{(-1.18, 0.0144, 0.3), (-1.18, 0.0165, 0.3)\}.$$

See Fig. 10 and the preparatory Fig. 9.

It is worth mentioning that our quadrangles are all far away from the 'lower curve' $\mathcal{C}_l^\ell$ whereas the quadrangles in Fig. 1 of Mischaikow and Mrozek [7] and in Fig. 3 of Galias and Zgliczynski [9] have a nonempty intersection both with $\mathcal{C}_0^u(z_0)$ and with $\mathcal{C}_0^\ell(z_0)$ (the notation in [7] and in [9] is different from ours.).

The rigorous ODE solver we use is the most current, Literate Programming C++ version[2] of the VNODE package developed by Ned Nedialkov [22]. Given an initial value on the Poincaré plane of equation $z = 0.3$ in $\mathbb{R}^3$, the solver computes interval enclosures of the exact solution at various time instances, including the endpoint of a prescribed time interval. When combined with an adaptive time and space subdivision algorithm, VNODE is able to compute small, codimension one interval enclosures of the intersection point between the exact trajectory and the Poincaré plane, i.e., tiny rectangles on the Poincaré plane containing the point of intersection.

For both data sets (16) and (17), condition (13) was checked on an eight core 3.4 GHz computer. The total CPU time was longer than two days. The program we used can be downloaded at https://github.com/dlazesz/chaos

Remark 2. It is plausible that the first part of Corollary 1 fails if Π_S^2 is replaced by Π_S. Similarly, we conjecture that Π_A^2 has no Σ_2-chaos on $\mathcal{C}_A^u$. The idea is to consider the numerical Lorenz-like maps $M_{I,1}^u, M_{I,2}^u, \ldots, M_{I,n}^u, \ldots$ one after the other, and to look for the minimum value of n for which condition (15) applies. The minimum value of n depends on whether $I = S$ or $I = A$.

Please see Figs. 11 and 12 portraying the numerical Lorenz-like maps $M_{S,1}^u, M_{S,1}^\ell$ and $M_{A,2}^u, M_{A,2}^\ell$, respectively. In each subfigure, the number of fixed points is less than two. Actually, Π_S and Π_A have no fixed points at all, and Π_A^2 has a unique fixed point in $\mathcal{C}_A^u$ and a unique fixed point in $\mathcal{C}_A^\ell$. Thus the existence of a conjugacy between Π_A^2 considered as a self-map of $\mathcal{C}_A^u$ (or as a self-map of $\mathcal{C}_A^\ell$) and the shift operator on the space of two symbols is excluded but semiconjugacies may still be possible.

5. Discussion

The approach of exploiting Lorenz-like maps in detecting chaos is tailored to (return maps associated to) Lorenz type attractors in $\mathbb{R}^3$. As a simple method of dimension reduction, it can hopefully be applied to diffeomorphisms in $\mathbb{R}^d$ having a hyperbolic structure with one expanding and $d-1$ contracting directions.

Everything becomes more complicated if the number of expanding directions is greater than one. Theorem 1 has been generalized to higher dimensions [23], and even to infinite dimension [24]. Nevertheless, the link between abstract theorems and real-world applications is not easy to find. While working at a faculty for informatics we find computer-assisted proofs for hyperchaos in circuit theory—a Chua–Roska neural network problem [25] (reconsidered also in our paper [26] a year later), a Chua circuit problem [27], a problem with memristors [28], all in four dimensions—particularly interesting.

Some kind of dimension reduction seems to play an indispensable role in all types of computer-assisted proofs for chaos we are aware of, especially in those more likely open to efficient automation in the future (adaptive set–oriented methods [29,30], reduction to constraint satisfaction algorithms [31,32]). The somewhat hidden role of unstable manifolds of saddle points in the earliest, by now classical computer-assisted proofs of chaos [6–9] is also an example of dimension reduction. For an explicit and algorithmic presentation, we recommend [33].

In addition to dimension reduction in computer-assisted proofs for chaos, the present paper is devoted to comparing various iterates of Poincaré return maps from the view-point of chaos theory. In general, the more the number of iterates, the more complicated the dynamics. The question on the minimum number of iterates for which semiconjugacies to the full shift are possible is, in our opinion, worth of further studying.

Acknowledgement

The authors are profoundly indebted to the referees for their comments, criticism, and helpful suggestions. Financial support for this work is gratefully acknowledged from the Science Foundation OTKA, No. 81403.

References

[1] Vallis GK. El Niño: a chaotic dynamical system? Science 1986; 232(4747):243–5.
[2] Vallis GK. Conceptual models of El Niño and the Southern Oscillation. J Geophys Res Oceans (1978–2012) 1988;93(C11):13979–91.
[3] Tung K. Topics in mathematical modelling. Princeton University Press; 2007.
[4] Sparrow C. The Lorenz equations. Bifurcations, chaos and strange attractors, Vol. 41. New York: Springer Verlag; 1982.
[5] Letellier C, Dutertre P, Gouesbet G. Characterization of the Lorenz system, taking into account the equivariance of the vector field. Phys Rev E 1994;49(4):3492.
[6] Mischaikow K, Mrozek M. Chaos in the Lorenz equations: a computer-assisted proof. Bull Am Math Soc 1995;32(1):66–72.
[7] Mischaikow K, Mrozek M. Chaos in the Lorenz equations: a computer assisted proof. Part ii: Details. Math Comput Am Math Soc 1998;67(223):1023–46.
[8] Zgliczyński P. Fixed point index for iterations of maps, topological horseshoe and chaos. Topol Methods Nonlinear Anal 1996;8(1): 169–77.
[9] Galias Z, Zgliczyński P. Computer assisted proof of chaos in the Lorenz equations. Physica D 1998;115(3):165–88.
[10] Gilmore R, Lefranc M. The topology of chaos: alice in stretch and squeezeland. John Wiley & Sons; 2002.
[11] Byrne G, Gilmore R, Letellier C. Distinguishing between folding and tearing mechanisms in strange attractors. Phys Rev E 2004;70(5): 056214.

[2] which can be downloaded from http://www.cas.mcmaster.ca/ nedialk/vnodelp/.

[12] Letellier C, Tsankov TD, Byrne G, Gilmore R. Large-scale structural reorganization of strange attractors. Phys Rev E 2005;72(2):026212.
[13] Letellier C, Roulin E, Rössler OE. Inequivalent topologies of chaos in simple equations. Chaos Solitons Fractals 2006;28(2):337–60.
[14] Sarachik ES, Cane MA. The El Niño-southern oscillation phenomenon. Cambridge University Press; 2010.
[15] Roy D, Musielak Z. Generalized Lorenz models and their routes to chaos. Part iii. Energy-conserving horizontal and vertical mode truncations. Chaos Solitons Fractals 2007;33(3):1064–70.
[16] Suarez MJ, Schopf PS. A delayed action oscillator for ENSO. J Atmos Sci 1988;45(21):3283–7.
[17] Battisti DS, Hirst AC. Interannual variability in a tropical atmosphere–ocean model: Influence of the basic state, ocean geometry and nonlinearity. J Atmos Sci 1989;46(12):1687–712.
[18] Krisztin T, The global attractor of slow oscillation for monotone negative feedback with time delay; in preparation.
[19] Mallet-Paret J, Sell GR. The Poincaré–Bendixson theorem for monotone cyclic feedback systems with delay. J Differ Equ 1996; 125(2):441–89.
[20] Umeki M. Chaos in the Battisti–Hirst original model for El Niño southern oscillation. Theor Appl Mech Jpn 2012;60:21–7.
[21] Bánhelyi B, Csendes T, Garay BM. Optimization and the Miranda approach in detecting horseshoe-type chaos by computer. Int J Bifur Chaos 2007;17(03):735–48.
[22] Nedialkov NS. Implementing a rigorous ODE solver through literate programming. In: Modeling, design, and simulation of systems with uncertainties. Springer; 2011. p. 3–19.
[23] Gidea M, Zgliczyński P. Covering relations for multidimensional dynamical systems. Part ii. J Differ Equ 2004;202(1):59–80.
[24] Wójcik K, Zgliczyński P. Topological horseshoes and delay differential equations. Discrete Contin Dyn Syst 2005;12(5):827–52.
[25] Yang X-S, Li Q. A horseshoe in a cellular neural network of four-dimensional autonomous ordinary differential equations. Int J Bifur Chaos 2007;17(09):3211–8.
[26] Bánhelyi B, Csendes T, Garay BM, Hatvani L. A computer-assisted proof of Σ_3-chaos in the forced damped pendulum equation. SIAM J Appl Dyn Syst 2008;7(3):843–67.
[27] Li Q, Hu S, Tang S, Zeng G. Hyperchaos and horseshoe in a 4D memristive system with a line of equilibria and its implementation. Int J Circ Theory Appl 2014;42:1172–88.
[28] Li Q, Tang S, Yang X-S. Hyperchaotic set in continuous chaos–hyperchaos transition. Commun Nonlinear Sci Numer Simul 2014; 19(10):3718–34.
[29] Mireles JJD. Adaptive set-oriented computation of topological horseshoe factors in area and volume preserving maps. SIAM J Appl Dyn Syst 2010;9(4):1164–200.
[30] Frongillo R, Treviño R. Efficient automation of index pairs in computational Conley index theory. SIAM J Appl Dyn Syst 2012; 11(1):82–109.
[31] Csendes T, Garay BM, Bánhelyi B. A verified optimization technique to locate chaotic regions of Hénon systems. J Global Optim 2006; 35(1):145–60.
[32] Goldsztejn A, Granvilliers L, Jermann C. Constraint based computation of periodic orbits of chaotic dynamical systems. In: Principles and practice of constraint programming. Springer; 2013. p. 774–89.
[33] Li Q, Yang X-S. A simple method for finding topological horseshoes. Int J Bifur Chaos 2010;20(02):467–78.